ADVANCED SUSTAINABLE SYSTEMS
www.advsustainsys.com

Ce^{3+}/Ce^{4+}–TiO_2 Nano-Octahedra as Active Photocatalysts for Ciprofloxacin Photodegradation Under Solar Light

Baliana Shani, Letizia Liccardo, Matteo Bordin, Isabel Barroso Martín, Antonia Infantes-Molina, Enrique Rodríguez-Castellón, Kassa Belay Ibrahim, Alberto Vomiero, and Elisa Moretti**

Cerium-containing titania nano-octahedra (CeTNOh) are obtained by ultrasonication-hydrothermal synthesis of Ce-containing titanate nanowires (0.35, 0.46, and 0.70 Ce mol %) from commercial TiO2 (Degussa P25). CeTNOh are tested as photocatalysts to degrade a target pollutant (ciprofloxacin) under simulated solar light and at mild conditions. CeTNOh are anatase polymorphs with increasing crystallite size as Ce content increases. Hydrothermal treatments enhance the specific surface area (SSA) compared to P25, although Ce addition slightly reduces SSA while increasing crystallite size. Electron Microscopy confirms the morphology, although higher Ce levels hinder a full transformation. X-ray photoemission spectroscopy (XPS) shows the presence of Ce^{3+}/Ce^{4+} redox pair, promoting electron mobility and Ti-Ce interactions. Optical and electronic spectroscopy reveals that Ce loading reduces the bandgap from 3.20 to 2.74 eV, extending light absorption into the visible range, thus enhancing the photocatalytic activity. The best sample, CeTNOh0.35, achieved 83% degradation of ciprofloxacin after 360 minutes under solar irradiation, with poor adsorption in the dark period. Higher Ce loadings negatively affect photoactivity by partially covering titania active sites. Reusability tests confirm the stability and efficiency of CeTNOh0.35 over three cycles, highlighting the importance of octahedral morphology in Ce-containing systems to boost the final photoactivity for water remediation.

1. Introduction

Nowadays, water contamination is one of the most pressing environmental issues to be faced, and special attention should be paid to persistent and hazardous organic molecules. Dyes and drugs are continuously released into water bodies, causing severe impacts on both the environment and human health.[1] Despite the low concentration in water ranging between 1 and 10 ng L^{-1}[2] antibiotics such as ciprofloxacin (CIP) have been considered contaminants of emerging concerns. In fact, they are ubiquitous and hardly degradable.[3] CIP is a synthetic antibiotic belonging to the class of fluoroquinolone and is gaining attention due to the increase in the bio-resistance of various bacteria, including the well-known *Escherichia Coli*.[4]

Conventional wastewater treatment processes, such as physical adsorption or separation by membranes, are considered low-cost and feasible techniques for the removal of various pollutants but unfortunately, the application is sometimes limited by the incomplete mineralization of the target molecules.[5] Furthermore, in the presence of wastewater containing mixtures of various complex

B. Shani[+], L. Liccardo, M. Bordin, K. B. Ibrahim, A. Vomiero, E. Moretti
Department of Molecular Sciences and Nanosystems
Ca' Foscari University of Venice
Via Torino 155, Venezia Mestre 30172, Italy
E-mail: alberto.vomiero@ltu.se; elisa.moretti@unive.it

I. B. Martín, A. Infantes-Molina, E. Rodríguez-Castellón
Department of Inorganic Chemistry
Crystallography and Mineralogy. Unidad Asociada al ICP-CSIC
Faculty of Sciences
University of Malaga
Campus de Teatinos, Malaga 29071, Spain

A. Vomiero
Division of Materials Science
Department of Engineering Sciences and Mathematics
Luleå University of Technology
Luleå 97187, Sweden

The ORCID identification number(s) for the author(s) of this article can be found under https://doi.org/10.1002/adsu.202400375

[+]Present address: Department of Inorganic Chemistry, University of Oxford, S Parks Rd, Oxford OX1 3QR, UK

© 2024 The Author(s). Advanced Sustainable Systems published by Wiley-VCH GmbH. This is an open access article under the terms of the Creative Commons Attribution License, which permits use, distribution and reproduction in any medium, provided the original work is properly cited.

DOI: 10.1002/adsu.202400375

organic molecules and byproducts, more specific treatment processes are demanded. In more detail, advanced oxidation processes (AOPs) are the leading alternative. AOPs involve the in-situ generation of short-lifetime reactive oxygen species (ROS), like hydroxy radicals (·OH), which are highly oxidative, electrophilic, and nonselective species able to mineralize a wide variety of toxic compounds.[6] Increasing interest has been drawn toward photochemical AOPs since among the most promising and sustainable methods for the removal of complex organic molecules in wastewater. This approach combines the use of a semiconductor as the photocatalyst with light irradiation. Titania (TiO_2), an n-type semiconductor, is one of the most studied and exploited photocatalysts for Ultraviolet (UV)-based AOPs thanks to its excellent properties, such as low toxicity, thermal and chemical stability, and outstanding oxidation power.[7] In general, after the creation of photo-excited electron and hole (e^--h^+) pairs, the photocatalytic reactions for the degradation of organic molecules in the presence of TiO_2 can be summarized as follows: 1) migration of e^--h^+ pairs onto the catalyst surface initiating redox reactions, 2) chain redox reactions with electron donor and electron acceptor, 3) charge-carriers trapping, and 4) recombination with subsequent energy dissipation.[8] Unfortunately, TiO_2 shows some major drawbacks including the fast charge carriers recombination (step 4 is favored over step 3) and the wide bandgap (i.e., 3.2 eV for anatase, the most photoactive crystalline phase).[9] Thus, only UV light, which represents ≈5% of the total solar radiation, can effectively excite electrons from the valence band (VB) to the conduction band (CB) of TiO_2 materials. However, several strategies such as morphology engineering or doping with metals and nonmetals, can be used to overcome these limits, extending the use of titania under the full solar light spectrum.[10] As widely reported in the literature, suitable nanostructures including nanowires, flakes, hollow spheres, nanoparticles, or nano-octahedra and nano-decahedra, combined with appropriate exposure of specific TiO_2 crystalline facets have demonstrated enhanced photocatalytic performances.[11] In detail, focusing on truncated decahedron and octahedron morphologies, the exposed (101) anatase facets seem to have a pivotal role in increasing the photocatalytic oxidation of organic compounds.[12] Additionally, the high photocatalytic activity of octahedral anatase crystals has been related to the presence of a well-crystallized surface with low-density defects that hinder or delay the recombination of photogenerated e^-–h^+ pairs.[13] As mentioned before, the doping of TiO_2 with either noble metals and their alloys with non noble metals like copper (Cu) [14] or the formation of heterostructures with reducible oxides like zirconia (ZrO_2) or ceria (CeO_2), has been reported to be efficient to enhance the catalytic performance. Specifically, coupling TiO_2 with CeO_2, cerium (III) oxide (Ce_2O_3), or cerium (Ce) ions seems to be a feasible strategy thanks to the promoted oxygen mobility induced by the Ce^{3+}/Ce^{4+} redox pair. For instance, Xu et al.[15] associated the superior photocatalytic activity of Ce- doped TiO_2 with the reduced recombination of e^-–h^+ pairs thanks to the presence of Ce^{4+} electron trapping sites. Moreover, doping with Ce ions has been often associated with a redshift in the main TiO_2 absorbance edge,[16] thus extending its absorption ability to the visible light region, which comprises more than 40% of the total incident solar spectrum.[17]

To the best of our knowledge, the use of TiO_2 nano octahedra containing Ce species for the photodegradation of antibiotics like CIP at mild operating conditions has not yet been studied.

Benefiting from the octahedral morphology and the Ce presence, the designed materials show an enhanced photoactivity toward CIP photodegradation in aqueous media under simulated solar light. The study focuses on assessing the role of both morphology and the presence of Ce containing species in the enhancement of photocatalytic activity of the pure TiO_2 for this specific photocatalytic process.

2. Results and Discussion

2.1. Morphology, Crystal Structure, and Textural Properties

As shown in **Figure 1a**, titatante nanowires (TNW) were hydrothermally synthesized, using a commercial P25 TiO_2 aqueous suspension under strong alkaline conditions. TNW were used as precursors for the second step to obtain titania nano-octahedra (TNOh) via an ultrasonication-hydrothermal synthesis. The introduction of Ce ions occurred during the first step, following the same procedure to obtain pure TNW. Upon step 1, the samples were labeled as CeTNWx, where Ce stands for cerium and x refers to the nominal mol% of 0.35, 0.46, and 0.70 mol.%. While following step 2, the samples were referred to as TNOh for pure titania nano-octahedra and CeTNOhx for Ce-doped samples. In this procedure, during the second hydrothermal treatment followed by calcination in air, a morphology rearrangement has occurred.

High-angle X-ray powder diffraction (XRPD) was performed to investigate the crystalline structure of both TNW and TNOh series of samples (Figure 1b,c). and the obtained patterns were compared to anatase TiO_2 (JCPDS PDF. #21-1272), CeO_2 (JCPDS PDF. #00-034-0394), and potassium hexatitanate ($K_2Ti_6O_{13}$) (JCPDS PDF. #40.0403) standard cards. As expected, the $K_2Ti_6O_{13}$ phase was found in TNW and CeTNWx samples, showing the typical diffraction peaks at 2θ (°) 11.48, 24.11, 29.25, and 47.89 (Figure 1b).

In Figure 1c, TNOh and CeTNOhx presented diffractograms with sharper and more intense peaks, suggesting higher crystallinity, compared to TNW. The presence of the anatase polymorph was confirmed by diffraction peaks observed at 2θ (°) 25.34°, 38.61°, 48.10°, 55.13°, 62.69°, and 68.76°. This indicates that after the second hydrothermal treatment, most of the $K_2Ti_6O_{13}$ is successfully converted into the highly photoactive phase anatase TiO_2.[8b] Indeed, all the TNOh series of samples showed the most intense peak at 2θ (°) 25.34° related to the (101) crystal plane that, according to Bragg's law, returns a d spacing of 0.35 nm, typical of the anatase phase. No presence of CeO_2 is detected in all the CeTNOhx samples, confirming the doping on the TiO_2 and excluding the formation of bulk secondary phases. The Scherrer equation was applied to estimate the anatase mean crystallite size for both TNW and TNOh (see **Table 1**).

Field emission-scanning electron microscopy (FE-SEM), High resolution-transmission electron microscopy (HR-TEM), and energy dispersive X-ray analysis-scanning transmission electron microscopy (EDX-STEM) were carried out to evaluate the size and the morphology and to analyze the elemental composition of the samples, respectively. As shown in Figure 1d (taken as a

© 2024 The Author(s). Advanced Sustainable Systems published by Wiley-VCH GmbH

RIGHTSLINK

23667486, 2024, 10, Downloaded from https://onlinelibrary.wiley.com/doi/10.1002/adsu.202400375 by Universita Ca' Foscari Venezia, Wiley Online Library on [30/10/2024]. See the Terms and Conditions (https://onlinelibrary.wiley.com/terms-and-conditions) on Wiley Online Library for rules of use; OA articles are governed by the applicable Creative Commons License

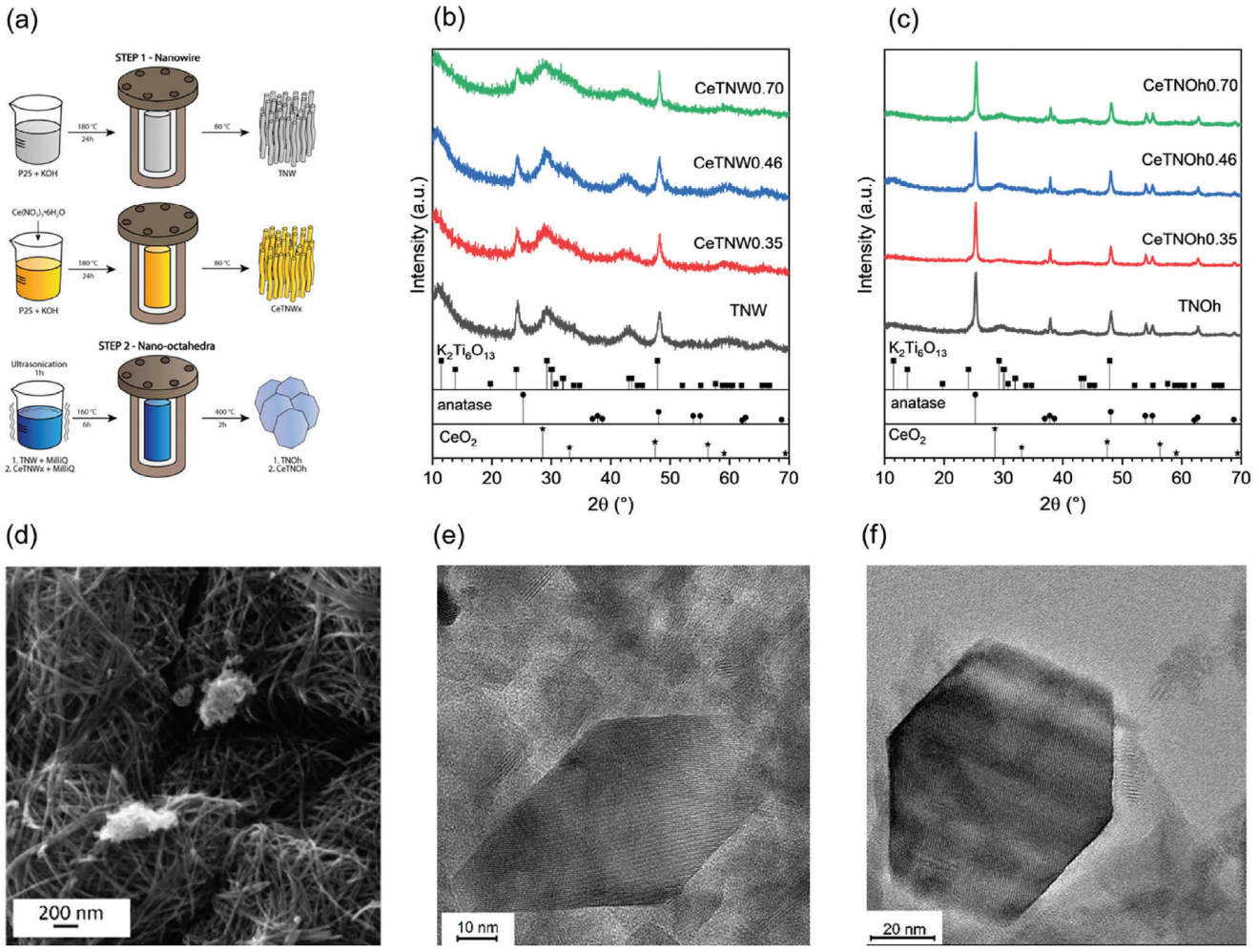

Figure 1. a) Graphical overview of the synthesis of the catalyst. Step 1 represents the hydrothermal synthesis of TNW and CeTNWx while step 2 represents the hydrothermal-ultrasonication synthesis of TNOh and CeTNOhx; b) High angle XRPD pattern for CeTNWx set; c) High angle XRPD pattern for CeTNOhx set; d) SEM image of TNW; HR-TEM micrographs of e) TNOh f) CeTNOh0.35.

Table 1. Summary of the mean crystallite size from the Scherrer equation, textural properties, and Brunauer-Emmet-Teller (BET) specific surface area (SSA) from nitrogen (N_2) isotherm analysis and bandgap (E_g) derived from the Tauc Plot for CeTNWx and CeTNOh sets.

Sample	Ce [mol%]	Mean crystallite size [nm]	[a] BET SSA [$m^2\ g^{-1}$]	[b] Pore Volume [$cm^3\ g^{-1}$]	[c] Pore Size [nm]	E_g [eV]
TNW	0.0	16	302	0.76	11.0	3.16
CeTNW0.35	0.35	17	357	0.96	14.6	3.07
CeTNW0.46	0.46	13	303	0.65	10.3	3.02
CeTNW0.70	0.70	33	355	0.93	13.3	2.99
TNOh	0.0	29	164	0.52	135	3.20
CeTNOh0.35	0.35	37	122	0.36	121	2.94
CeTNOh0.46	0.46	43	198	0.50	113	2.95
CeTNOh0.70	0.70	39	194	0.53	107	2.74
P25	–		61	0.10	6.8	3.20
Anatase	–		85	0.19	10.1	3.10

[a] N_2 physisorption values obtained at −196 °C with BET method by N_2 physisorption at −196 °C; [b] Single point adsorption total pore volume of pores calculated at relative pressure $P/P_0 = 0.94$ by N_2 physisorption at −196 °C; [c] Barrett-Joyner Halenda (BJH) desorption average pore width by N_2 physisorption at −196 °C.

© 2024 The Author(s). Advanced Sustainable Systems published by Wiley-VCH GmbH

RIGHTSLINK
23667486, 2024, 10, Downloaded from https://onlinelibrary.wiley.com/doi/10.1002/adsu.202400375 by Universita Ca' Foscari Venezia, Wiley Online Library on [30/10/2024]. See the Terms and Conditions (https://onlinelibrary.wiley.com/terms-and-conditions) on Wiley Online Library for rules of use; OA articles are governed by the applicable Creative Commons License

representative), P25 was successfully converted into TNW and CeTNWx during the hydrothermal treatment (step 1 Figure 1a; Figure S1, Supporting Information).

All TNW and CeTNW samples showed uniform, randomly distributed partially proton exchanged potassium titanate nanowires. Notably, CeTNW0.46 showed some changes in the nanowires length and diameter. Specifically, the presence of Ce ions led to a decrease in the nanowires length from 86 to 71 nm and a reduced diameter from an average value of 7 nm in pure TNW to 5 nm (Figure S2, Supporting Information).

EDX mapping for CeTNW0.46 is reported in Figure S3(Supporting Information). Elemental analysis showed the presence of homogeneously distributed Ce and as expected, potassium (K), oxygen (O), and titanium (Ti) related to the $K_2TI_6O_{13}$ (observed by XRPD analysis).

As observed by HR-TEM images (Figure 1e,f) and TEM images in Figure S4, Supporting Information), after the second hydrothermal treatment (step 2 Figure 1a), the pure and Ce-containing samples presented well-defined octahedral nanoparticles. Pure TNOh showed an average length of 63 nm and width of 31 nm. The size of TNOh increased with Ce loading. In detail, the length and width were 71 and 37 nm for the CeTNOh0.35 sample and 91 and 45 nm for CeTNOh0.46, respectively. The size distributions were calculated by ImageJ software analysis (Figure S4, Supporting Information). As already detected for CeTNWx, EDX-STEM analyses (Figure S5, Supporting Information) showed the presence of homogeneously dispersed Ce inside the CeTNOhx matrix without the formation of any aggregates.

Nitrogen (N_2)-physisorption at −196 °C (Figure S6a,b, Supporting Information) and the Brunauer-Emmet-Teller (BET) analysis (Table 1) were performed to assess textural properties, porosity, and specific surface area (SSA) of the samples in comparison with commercial P25 (Degussa) used as precursor, and commercial Anatase TiO_2 (from Sigma–Aldrich).

According to the IUPAC classification[18] the synthesized TNW, TNOh, and the relative Ce-containing samples exhibited Type-IV isotherms with H3 hysteresis loop typical of mesoporous materials. The hydrothermal process is beneficial for increasing the SSA of TNW.[19] In fact, TNW and CeTNWx precursors presented a high SSA ranging from 357 to 302 $m^2\ g^{-1}$ and pore volume of 0.65–0.96 $cm^3\ g^{-1}$, higher than the commercial P25 TiO_2 (61 $m^2\ g^{-1}$ and 0.10 $cm^3\ g^{-1}$). The observed enhancement of textural properties cannot be systematically correlated with the increase in Ce content. Nevertheless, at low loading (0.35 mol.%) the detectable increase of SSA and pore volume can be associated with interparticle spaces.[20] As a consequence of the hydrothermal treatment and subsequent calcination, TNOh and CeTNOhx samples showed lower SSA compared to the TNW and CeTNWx precursors. Indeed, thermal treatments are associated with crystal growth (as evidenced by XRPD results, Table 1) and impoverishment of textural properties compared to the noncalcined precursors.[21] However, the recorded SSA for TNOh samples and their Ce-containing counterparts ranged between 164 and 198 $m^2\ g^{-1}$, at least three times higher than the SSA of P25 (Degussa).

2.2. Ce-Presence Effects on the Surface Chemical Composition

Ce content was investigated by the synergic use of Rutherford Backscattering spectrometry (RBS) to follow the Ce profile within the samples and to obtain the Ce:Ti atomic ratio, and high-resolution X-ray photoelectron spectroscopy (XPS) to study the surface chemical composition.

RBS was carried out following the Ce profile in the samples to investigate the Ce content of the mixed Ce-Ti samples and to obtain the Ce:Ti atomic ratio. The RBS spectra for both TNOh and CeTNOhx samples are reported in Figure S7 (Supporting Information). A homogeneous Ce concentration was detected for all CeTNOhx samples (Figure S7b, Supporting Information) with a maximum Ce:Ti atomic ratio of 0.005:1 for CeTNOh0.70. As expected, no Ce species were detected in the TNOh sample.

Concerning X-ray photoemission spectroscopy (XPS) analysis, high-resolution Ti 2*p*, O *1s*, and Ce 3*d* core level spectra for both TNW/CeTNWx and TNOh/CeTNOhx are reported in **Figures 2** and **3**, respectively. The survey spectra for CeTNW0.46) and CeTNOh0.70, as an example, have been reported in Figure S8 (Supporting Information).

The Ti *2p* core level spectra, in Figure 2a,c, can be fitted with the typical asymmetric doublet indicating the presence of Ti^{4+} species for both TNW/CeTNWx and TNOh/CeTNOhx series. In fact, the peaks at ≈458.7 and 464.4 eV were assigned to Ti *2* $p_{3/2}$ and Ti *2* $p_{1/2}$, respectively, which showed a separation of 5.7 eV, normally ascribed to octahedrally coordinated Ti^{4+} ions.[22] As already reported in the literature, the slight variations in the binding energy between the main Ti *2* $p_{3/2}$ peaks at 458.7 eV for TNW/CeTNWx and 458.3 eV for TNOh/CeTNOhx, can be related to the higher interactions between Ce and Ti species within the samples.[23]

When increasing the Ce content in CeTNWx, a shift to lower binding energy is observed. The possibility of exchanging cations in the titanate with K^+ and Ce^{3+} has previously been reported,[24] thus the shift could be associated with the partial substitution of K^+ by Ce^{3+} within titanate crystal lattice and the consequent formation of Ti—O—Ce bonds.[25] Conversely, with the increase in Ce content, the Ti $2p_{3/2}$ peak for CeTNOhx slightly shifted toward higher binding energies. In this case, the presence of Ce may lead to higher mobility of electrons at the core level, as it is supported by previous reports.[22a,26]

Considering O *1s* core level spectra (Figure 2b,d) for both TNW/CeTNWx and TNOh/CeTNOhx sets, three main components were needed to describe the samples. In TNW and CeTNWx samples, the main peak at ≈530.3 eV is related to oxygen from the TiO_2 lattice, while the second peak at ≈531.3 eV belongs to the surface adsorbed oxygen, defect oxide states, and hydroxyl groups (OH) bonded to Ti. The last component at higher binding energies in the range 532.5–533.5 eV (533.5 eV for TNW, 532.5 eV for CeTNW0.35, 532.8 eV for CeTNW0.46, and 532.6 eV for CeTNW0.70) can be attributed to adsorbed water (H_2O) molecules on the catalysts surface.[22a,27] In CeTNWx, as already discussed for Ti *2p* core level spectra, at higher Ce loadings the main contribution associated with lattice oxygen at ≈530.3 eV is shifted to lower binding energy. In the case of TNOh and CeTNOhx, the main contribution due to lattice oxy-

© 2024 The Author(s). Advanced Sustainable Systems published by Wiley-VCH GmbH

RIGHTSLINK

23667486, 2024, 10, Downloaded from https://onlinelibrary.wiley.com/doi/10.1002/adsu.202400375 by Universita Ca' Foscari Venezia, Wiley Online Library on [30/10/2024]. See the Terms and Conditions (https://onlinelibrary.wiley.com/terms-and-conditions) on Wiley Online Library for rules of use; OA articles are governed by the applicable Creative Commons License

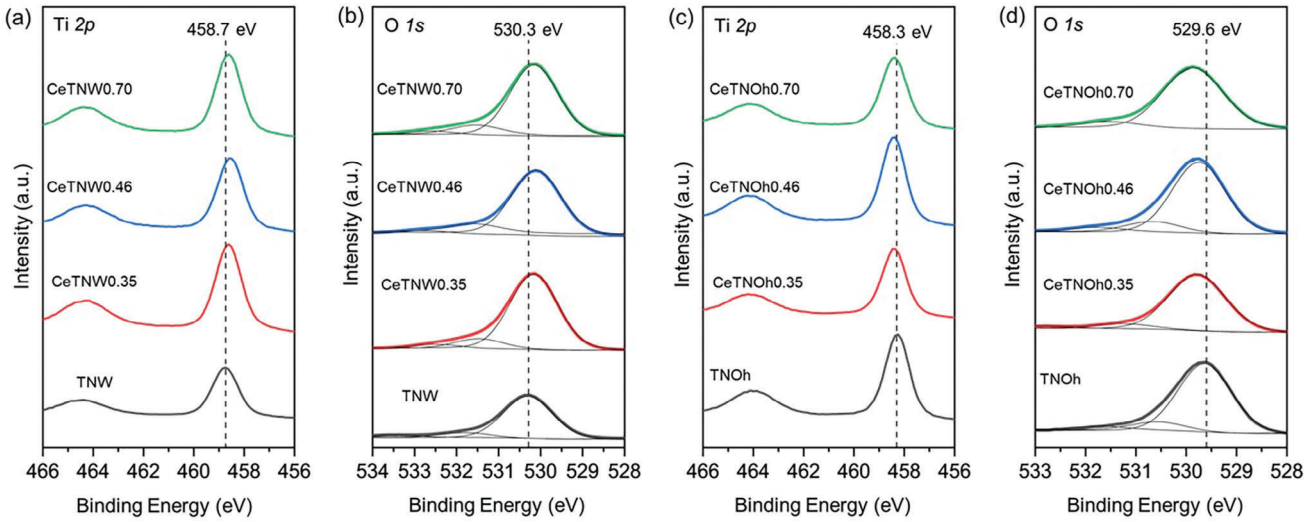

Figure 2. a,b) XPS spectra for (a) Ti 2*p* core level spectra and (b) O 1s core level spectra for TNW/CeTNWx sets of catalysts; c) Ti 2*p* core level spectra and d) O 1s core level spectra for TNOh/CeTNOhx sets of catalysts.

gen is located at lower binding energy, ≈529.8 eV, suggesting an increase in the contribution from CeO_2 species and the formation of CeO_2-TiO_2 phase on the surface after the second step of the synthesis.[28] When the Ce loading from the precursor increases, a shift toward higher binding energies is observed, indicating an increased number of adsorbed reactive oxygen species with higher mobility.[29] It is visible that the intensity of the last component at 532.5–533.5 eV (associated with superficially adsorbed H_2O)/decreased in TNOh/CeTNOhx samples compared to TNW/CeTNWx samples. This can be ascribed to the second step of the synthesis which included the calcination procedure, leading to a loss of superficially adsorbed water molecules.

Ce 3*d* core level spectra in Figure 3 display a high signal-to-noise ratio due to the low metal loading. However, the contributions related to the presence of Ce^{3+}/Ce^{4+} are detected for both the CeTNWx and CeTNOhx series of samples, especially at higher Ce-loading. The following spin-orbit doublets associated with Ce^{4+} species are detected: v (≈882.7 eV) and u (≈901.3 eV); v″ (≈888.5 eV), and u″ (≈907.3 eV); v‴ (≈898.3 eV) and u‴ (≈916.9 eV), the latter being satellite peaks associated with tetravalent Ce in Ce compounds.[26] On the other hand, the Ce^{3+} presence is also observed, which is associated with high binding energy doublets v' (≈885.2 eV) and u' (≈903.4 eV) and lowest binding energy states v_0 (≈880.9 eV) and u_0 (≈899.2 eV).[30]

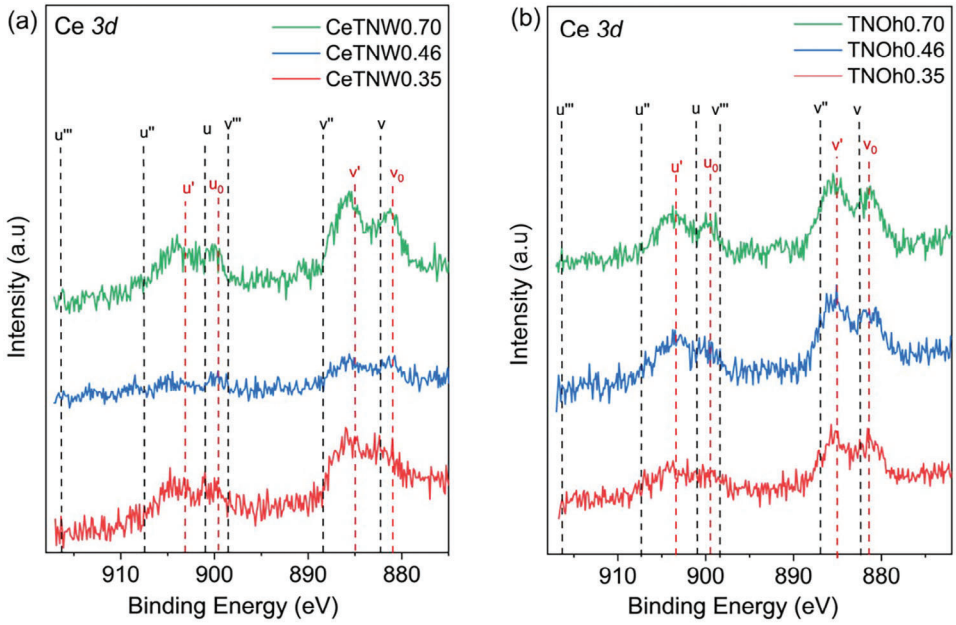

Figure 3. a,b) XPS spectra for Ce 3*d* core level spectra for (a) TNW/CeTNWx and (b) TNOh/CeTNOhx sets of catalysts.

© 2024 The Author(s). Advanced Sustainable Systems published by Wiley-VCH GmbH

RIGHTSLINK

23667486, 2024, 10, Downloaded from https://onlinelibrary.wiley.com/doi/10.1002/adsu.202400375 by Universita Ca' Foscari Venezia, Wiley Online Library on [30/10/2024]. See the Terms and Conditions (https://onlinelibrary.wiley.com/terms-and-conditions) on Wiley Online Library for rules of use; OA articles are governed by the applicable Creative Commons License

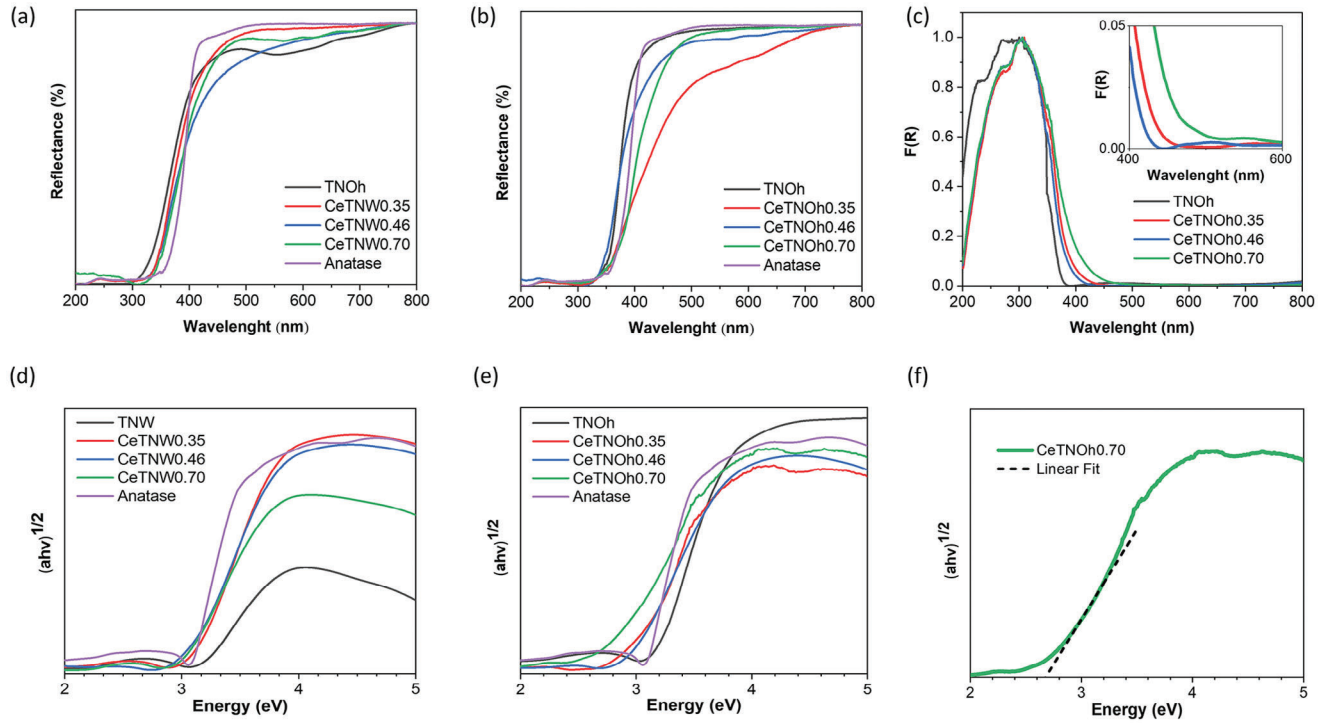

Figure 4. a,b) DRUV-Vis spectra for (a) CeTNWx and (b) CeTNOhx sets; c) F(R) spectra for CeTNOhx sets in dimensionless units from the Kubelka Munk Fuction; d,e) Tauc plots for (d) CeTNWx and (e) CeTNOhx sets; f) Extrapolation of the E_g (eV) for CeTNOh0.70 taken as an example.

The intensity of Ce^{3+}-related peaks increased with the increase in the Ce-loading, indicating a stronger electronic interaction between Ce and Ti.[31] Noteworthy, the signals are more intense in the CeTNOhx set of catalysts, suggesting the presence of a higher number of superficially exposed Ce species (Figure 3b).

The K 2p core level spectra for both CeTNWx and CeTNOhx sets have been included in the SI file (Figure S9, Supporting Information). No significant changes can be appreciated neither with Ce loading nor with structural changes from TNW/CeTNWx to TNOh/CeTNOhx. Two peaks are observed, associated with K $2p_{3/2}$ and K $2p_{1/2}$ spin orbit doublets at 292.6 and 295.2 eV, respectively, which have been previously attributed to K^+ in potassium titanates.[32]

2.3. DRUV-Vis and PL Spectroscopy

As widely reported in the literature, the coexistence of Ce^{3+}/Ce^{4+} species in Ce-Ti systems seems to promote photocatalytic activity thanks to their electron transfer properties that favor the separation of photogenerated electrons and holes.[22b] Thus, to further study the charge-carriers dynamic and the photo-responsive behavior of the prepared materials, Diffuse reflectance UV-Visible (DRUV-Vis) spectra and Photoluminescence (PL) spectra were acquired. The collected DRUV-Vis spectra, Tauc plots and Optical absorption or F(R) spectra from the Kubelka Munk Function for the prepared samples, and the benchmark Sigma–Aldrich Anatase are shown in **Figure 4**. Bandgap values were calculated from Tauc Plots, using the intercept of the extrapolated linear fit and they are collected in Table 1 for both TNW/CeTNWx and TNOh/CeTNOhx series of samples.

Pure TNW and TNOh samples presented the typical absorption edge of TiO_2 materials at ≈400 nm, related to the wide absorbing bandgap in the UV region.[33] From Figure 4a,b, it can be observed that the Ce introduction results in a redshift of the main absorbance edge, particularly pronounced in the TNOh/CeTNOhx series. This can be associated with the formation of Ce^{3+} species, which introduce some localized mid-gap states within the bandgap of the TiO_2 semiconductor.[34] Confirming that doping is an efficient strategy to shift the absorption toward the visible region.

This is more evident in CeTNOhx F(R) spectra in Figure 4c. All samples showed the typical TiO_2 strong absorption band in the UV region centred at ≈310 nm, broader for pure TNOh. Furthermore, in CeTNOhx, the clear redshift of the main band edges can be associated with the $4f$ to $5d$ transition of Ce^{3+} in the ligand environment of O_2^- surrounding TiO_2 nanoparticles. Thus, the predominance of Ce^{3+} instead of Ce^{4+} is further confirmed. In fact, the Ce ion in the +4 state does not contain any electron and no transition occurs from the electronic configuration of the ground state ($4f^0 5d^0$).[35] As expected, the observed redshift influences the bandgap values (E_g (eV)), decreasing from 3.2 eV in pure TNW to 2.99 eV in samples with the highest Ce loading (Figure 4d–f; Figure S10, Supporting Information). This decrease is more pronounced in CeTNOhx catalysts, where the E_g(eV) lowers from 3.2 eV for the pure TNOh sample to 2.74 eV for the CeTNOh0.70 counterpart. All the calculated E_g(eV) values are in accordance with values for Ce containing nanostructures already reported in the literature.[36]

© 2024 The Author(s). Advanced Sustainable Systems published by Wiley-VCH GmbH

RIGHTSLINK

23667486, 2024, 10, Downloaded from https://onlinelibrary.wiley.com/doi/10.1002/adsu.202400375 by Universita Ca' Foscari Venezia, Wiley Online Library on [30/10/2024]. See the Terms and Conditions (https://onlinelibrary.wiley.com/terms-and-conditions) on Wiley Online Library for rules of use; OA articles are governed by the applicable Creative Commons License

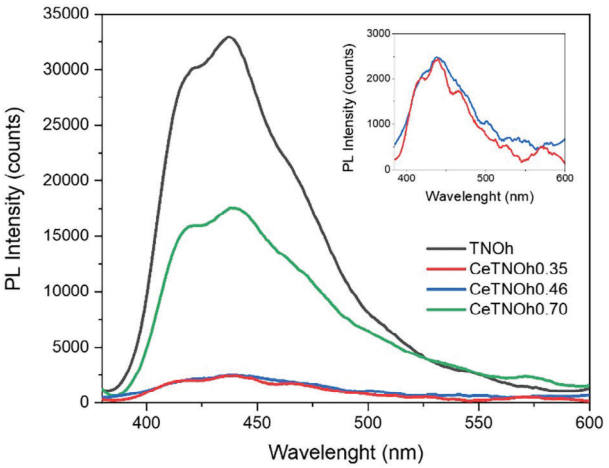

Figure 5. PL spectra for CeTNOhx set.

PL spectra for both pure TNOh and CeTNOhx catalysts were collected by exciting the materials at 350 nm, using a cut-off filter at 370 nm. As can be noticed in **Figure 5**, undoped TNOh exhibit a strong emission band in the range between 380 and 600 nm, containing several emission peaks. A nonuniform emission trend is observed as the dopant content increases. Up to the optimal doping limit (0.46 mol %), luminescence energy can be transferred among Ce^{3+} ions, resulting in quenching of luminescence, thus hindering charge-carriers recombination. Instead, as the doping concentration increases, the dopant itself may act as a radiative recombination centre, thus increasing the charge-carriers recombination rate and consequently, the PL intensity.

2.4. Photocatalytic Test: CIP Degradation Under Simulated Solar Light

The photocatalytic activity under simulated solar light irradiation, in an aqueous solution and at room temperature, was evaluated for TNOh and all the CeTNOhx samples, following the degradation of CIP as the target molecule. Kinetic studies were performed measuring the typical CIP main absorbance peak at 272 nm, starting from the photolysis under solar light after 360 min of exposure.

In **Figure 6a**, the monitoring of DRUV–vis spectra of CIP degradation under dark conditions (30 min) and during solar light irradiation when using the bare TNOh sample (360 min), is displayed as an example. Here, the mineralization of the drug can be observed as the reaction takes place. Figure 6b displays the photocatalytic degradation of CIP as a function of irradiation time with and without catalysts under simulated solar light. CIP is significantly stable over sunlight irradiation, in fact, the final concentration over the initial concentration (C/C_0) curve decreased slightly during the whole reaction time. After equilibration in the dark, CIP was partially adsorbed on the surface of photocatalysts with a decrease in its concentration of 20% for each sample except CeTNOh0.70, which was adsorbing almost 34% of the target molecule. This can be associated with the higher amount of CeO_2 on the surface of the sample as observed in the XPS results, which can interact better with CIP molecule.[37] When photocatalysts were added to the system, a decrease in C/C_0 was detected with increasing irradiation time. All the samples show a very good photocatalytic activity, but the sample with the best performance is CeTNOh0.35, being able to degrade 83% of the drug within the exposure time. For comparison purposes, in Table S1 (Supporting Information), we report the activity of state-of-the-art semiconductor-based catalysts for CIP photodegradation. Additionally, for CeTNOh0.35 the apparent kinetic constant of 9.9×10^{-3} min^{-1} is higher than the bare TNOh kinetic constant $k_{TNOh} = 7.85 \times 10^{-3}$ min^{-1}, confirming what already stated (Figure 6b). Doping the TiO_2 matrix is a good strategy to increase the photodegradation ability, by broadening the absorbance toward the visible range of bare TiO_2 and lowering its bandgap energy, overall reducing the e^--h^+ recombination rate. The superior photocatalytic activity in composite systems is widely attributed in literature to the Ce^{3+}/Ce^{4+} electron transfer properties, which enhance charge-carrier separation.[38] The efficiency of the dopant toward the trapping of charge carriers is strictly related to the concentration and distribution of the dopants, and the stability of the TiO_2 crystalline phase. Thus, it is extremely important to reach an optimal amount of Ce loading. Interestingly, the higher the dopant content, the lower the photocatalytic activity is among the doped samples. Indeed, the CeTNOh0.70 sample is the least active for CIP degradation. Despite its increased capacity as a solar light harvester compared to TNOh, the presence of Ce ions at 0.70 mol.% and increasing CeO_2 content on the surface is causing a decrease in the photocatalytic activity, reinforcing the crucial role of morphology and composition in the photoactivity of the prepared samples. Free radicals trapping experiments were useful to investigate the main active species responsible for CIP degradation in the presence of the CeTNOh0.35 photocatalyst (Figure 6d). In fact, it is possible to estimate the main active species during the photodegradation reaction by introducing in the system three selected scavengers in the same photocatalytic conditions used before. In detail, oxalic acid (OA), tert-butanol (tBuOH), and N_2were used as holes (h^+), OH, and superoxide (O_2^-) scavengers, respectively. The photocatalytic activity is considerably inhibited when OA (h^+ scavenger) is added, while the addition of tBuOH (OH scavenger) is hardly affecting the overall activity. Hence, h^+ should be the major reactive species involved in the CIP degradation by the investigated sample under simulated solar light irradiation. Finally, stability and reusability tests were performed (**Figure 7**). As can be noticed, after 3-cycle reusability tests, CeTNOh0.35 is still active and the percentage value of degraded CIP remained unchanged, confirming the stability of the system and the possibility of effectively recovering the photocatalyst from the slurry.

3. Conclusion

In this work, an ultrasonication-hydrothermal route synthesis was proposed to obtain Ce^{3+}/Ce^{4+}-doped TiO_2 nano-octahedra with 0.35, 0.46, and 0.70 Ce mol.% loading. HR-TEM and XRD analyses confirmed the octahedral morphology and the anatase phase, with the most intense peak corresponding to the (101) crystal planes. STEM-EDX and XPS analysis validated the presence of homogeneously dispersed Ce ions in the TiO_2 matrix and surface, while the amount of CeO_2 on the surface increased with higher doping. BET measurement confirmed that

© 2024 The Author(s). Advanced Sustainable Systems published by Wiley-VCH GmbH

RIGHTSLINK

23667486, 2024, 10, Downloaded from https://onlinelibrary.wiley.com/doi/10.1002/adsu.202400375 by Universita Ca' Foscari Venezia, Wiley Online Library on [30/10/2024]. See the Terms and Conditions (https://onlinelibrary.wiley.com/terms-and-conditions) on Wiley Online Library for rules of use; OA articles are governed by the applicable Creative Commons License

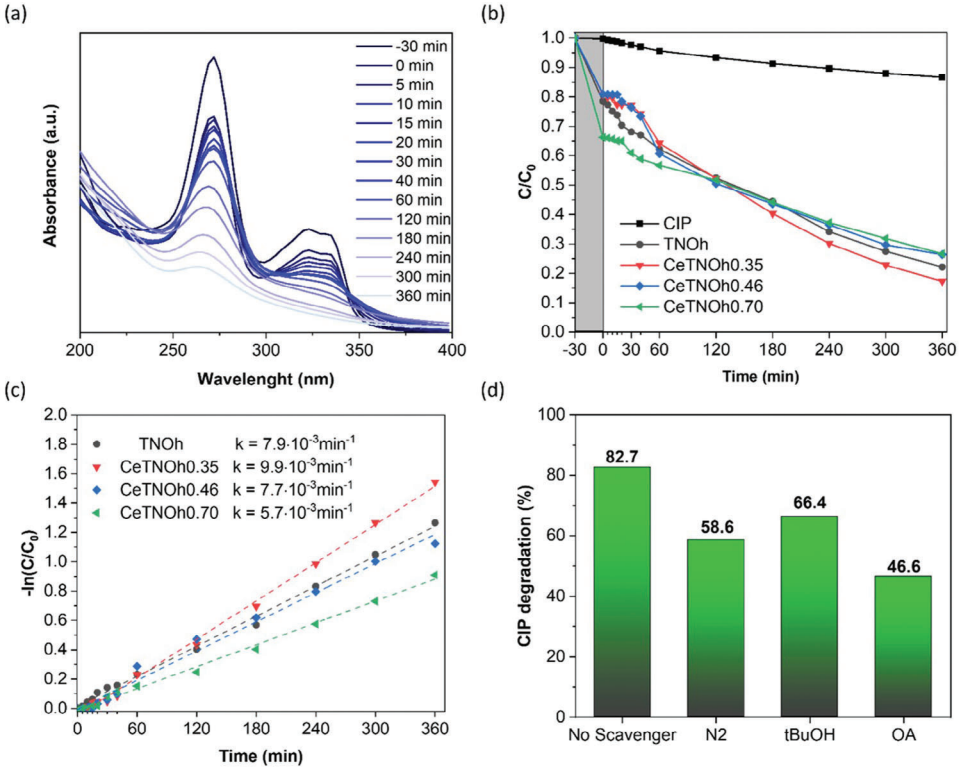

Figure 6. a) DRUV–vis absorption spectra recorded at different times, from 30 min under dark conditions to 360 min under simulated solar light irradiation, for the TNOh sample; b) Photocatalytic degradation of CIP as a function of irradiation time with and without catalysts (CIP curve) under simulated solar light irradiation. c) CIP degradation kinetics with linear fits of the experimental data in dashed lines. d) Free radical trapping experiments results for CeTNOh0.35 photocatalyst.

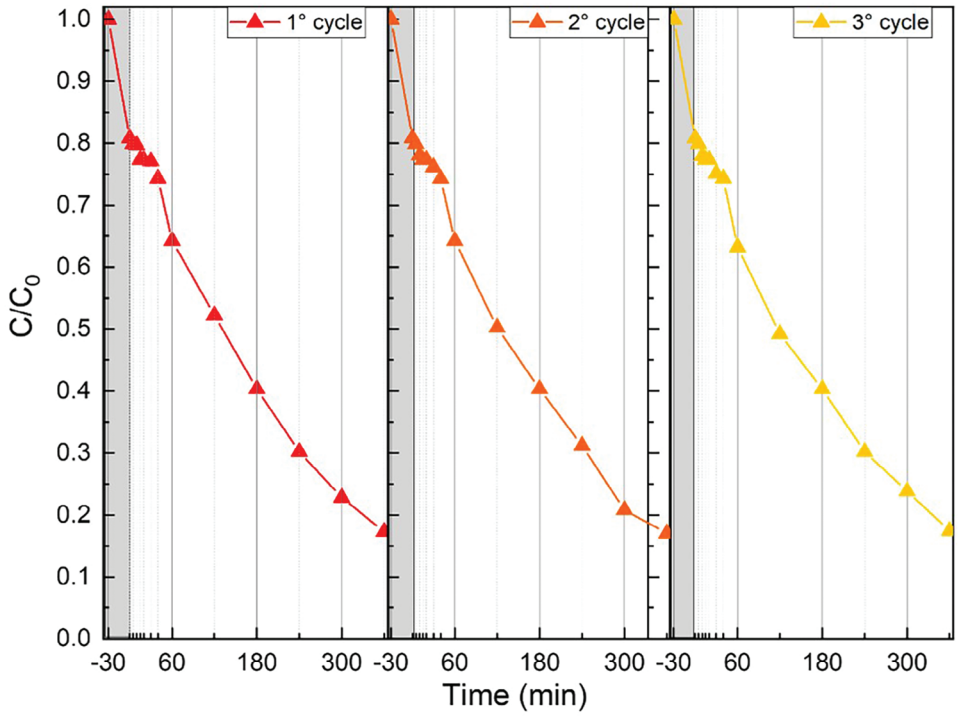

Figure 7. 3-Cycles reusability test of the best performing sample CeTNOh0.35.

© 2024 The Author(s). Advanced Sustainable Systems published by Wiley-VCH GmbH

RIGHTSLINK

23667486, 2024, 10, Downloaded from https://onlinelibrary.wiley.com/doi/10.1002/adsu.202400375 by Universita Ca' Foscari Venezia, Wiley Online Library on [30/10/2024]. See the Terms and Conditions (https://onlinelibrary.wiley.com/terms-and-conditions) on Wiley Online Library for rules of use; OA articles are governed by the applicable Creative Commons License

the TNOh/CeTNOhx samples are mesoporous materials with a very high SSA, going from 122 to 194 $m^2\ g^{-1}$, at least two times higher than that of commercial anatase.

These TNOh/CeTNOhx were evaluated as photocatalysts for ciprofloxacin (CIP) degradation in water under simulated solar-light irradiation at room temperature and atmospheric pressure. As a result, outstanding CIP degradation up to more than 80% after 360 min of reaction is promoted by the faceted morphology and Ce doping. The presence of cerium species improved the photo response of the TNOh/CeTNOhx, where the highest doping (0.70 Ce mol.%) induced a decrease in the starting bandgap of titania up to 2.75 eV. Overall, upon Ce ions addition a redshift of the absorption edge was observed along with the formation of oxygen vacancies (induced by the Ce^{3+} /Ce^{4+} redox pair). PL measurements confirmed that the presence of cerium in the octahedral system leads to the quenching of electron-hole recombination. In the context of CIP photodegradation, the main active species are holes. The best performing catalyst was CeTNOh0.35, suggesting that very low Ce concentrations are beneficial for the targeted reaction and influence the adsorption-degradation equilibrium. At higher doping, larger amounts of CeO_2 covering the surface (confirmed by XPS measurements) seem to weaken the interaction with the active phase TiO_2, while only boosting CIP absorption rather than degradation. The reusability test of the CeTNOh0.35 catalyst showed that Ce-doped nano-octahedra were still active and stable in the CIP drug degradation under simulated solar light after three cycles, which demonstrates the stability of the prepared photocatalysts. To the best of our knowledge, the present research is the first example of $Ce^{4+}/Ce^{3+}-TiO_2$ octahedral nanostructures, shedding light on the cooperation between octahedral morphology for TiO_2 and enhanced optical as well as surface properties in the presence of low Ce concentration. In the context of solar light-induced photodegradation, we anticipate that these new sets of materials are promising candidates for wastewater treatment.

4. Experimental Section

Catalysts Synthesis: The catalysts were synthesized by modifying a hydrothermal-ultrasonication route reported by Wei and co-workers.[39] First, potassium titanate nanowires (TNW) were synthesized as precursors to obtain nano-octahedra (TNOh). In a typical procedure, 50.49 g of potassium hydroxide (KOH) were dissolved in 90 mL of Milli-Q water under stirring, to prepare a 10 M KOH solution. The pH was controlled using a calibrated pH meter. The solution was prepared under a fume hood and appropriate PPE were used. After dissolution, 0.9 g of commercial titania (Degussa P25) were added and the suspension was stirred for 1 h. The final solution was then transferred to a Teflon-lined autoclave, and a hydrothermal reaction was performed at 180 °C for 24 h in an oven. The resulting powder was recovered by filtering under vacuum and washed with Milli-Q water, 0.1 M HNO_3 solution and finally, with hot Milli-Q water until neutral pH was reached. As final step, the TNW were dried at 80 °C for 12 h. The introduction of Ce ions in the precursor system followed a doping strategy. To hydrothermally synthesize Ce-doped TNW, a given amount (0.35, 0.46, and 0.70 mol.% where mol.% = Ce/ Ce + Ti) of cerium nitrate aqueous solution (Ce $(NO_3)_3{\cdot}6H_2O$, Sigma–Aldrich, 95%) was added to the stirring suspension of P25 in 10 M KOH after 30 min of stirring (see Figure 1a). This suspension was stirred for another 30 min and afterward added into an autoclave and the same procedure as for the pure TNW sample was followed. The samples were named CeTNWx, where Ce stands for cerium and x refers to mol% doping of 0.35, 0.46, and 0.70 mol.%.

In the second step, octahedral anatase nanoparticles were obtained from TNW and CeTNWx samples. In a typical synthesis, nanowire precursors were ultrasonically dispersed in Milli-Q water for 1 h at room temperature, and the suspension was transferred to an autoclave for the hydrothermal reaction at 160 °C for 6 h. After the reaction was completed, the solid product was recovered by centrifugation and dried under vacuum at 80 °C for 12 h. Finally, the dried solid was calcined at 400 °C for 2 h with a heating rate of 1 °C min^{-1} in static air. The samples were named TNOh for pure titania nano-octahedra and CeTNOhx for cerium-containing samples where x refers to the nominal cerium mol % doping of 0.35, 0.46, and 0.70 mol.%.

In the potassium hexatitanate ($K_2Ti_6O_{13}$) structure, the titanium is octahedrally coordinated and the octahedral TiO_6 shares an edge in a 1D structure.[40] The transformation of the titanate into the anatase phase can proceed in two ways. The first is the dissolution-recrystallization mechanism. When the potassium titanate structure dissolves, titanium hydroxide intermediate species are formed thanks to the interaction with OH- groups in solution which undergo condensation and subsequent recrystallization.[41] In the second, a topotactic reaction occurs. In this case, there is the condensation of —TiOH species and rearrangement of the TiO_6 octahedra. Hydrothermal reactions in acqueous solutions either at neutral pH or slightly acidic do favour the latter mechanism over the dissolution-recrystallization pathway.[42] In all cases, the recrystallization process is influenced by the pH and reaction temperature. Solutions with pH values in the range of 3.4–8.2 and temperatures below 200°C favor the anatase phase, well in accordance with the reaction conditions (160 °C, Milli Q water).[43]

Characterization Techniques: X-Ray powder diffraction (XRPD) patterns were collected using a Philips PW 1319 diffractometer with a voltage of 40 kV, with Bragg–Brentano reflection configuration and a Cu anode (Kα1 = 1.5406 Å), recording in the range from 10° to 80° of 2θ, with 0.05° of step size. Crystallite sizes have been estimated using the Scherrer equation.

Nitrogen adsorption-desorption isotherms at −196 °C were performed with an ASAP 2420 apparatus of Micromeritics. Before analysis, the samples were outgassed at 150 °C for 24 h. The Brunauer–Emmet–Teller (BET) method was applied to obtain the specific surface area or SSA. Pore volume was calculated at the relative pressure $P/P_0 = 0.94$ and pore size distribution was calculated by the Barrett-Joyner-Halenda or BJH method.

High-resolution scanning electron microscopy (SEM) images were collected with a FEG-SEM ZEISS SUPRA 40 apparatus with 30 kV acceleration voltage, equipped with a field emission cathode as an electron source and SE2, InLens and STEM detectors. Transmission electron microscopy (TEM) micrographs were obtained with a TALOS F200x instrument working at 200 kV and 5.5 µA. In addition, scanning transmission electron microscopy (STEM)images were registered with an annular dark field or HAADF detector at 200 kV and 200 pA. ImageJ software (ImageJ 1.51K) was used to estimate mean particle size.

X-ray photoemission spectroscopy (XPS) measurements were carried out in a PHI 5700 Physical Electronics spectrometer, with nonmonochromatic Mg Kα radiation equipped with a multichannel detector. Spectra were collected with PHI ACCESS ESCA-V6.0 F software and a constant step mode of 29.35 eV. Binding energy values were referred to the C 1s peak of the adventitious carbon contamination layer (284.8 eV) and the error in binding energy values was estimated to be ±0.1 eV. Recorded data were analyzed with Multipak 9.5 software.

Diffuse reflectance Ultraviolet-Visible spectra (DRUV-Vis) were collected in a Cary UV–vis spectrometer equipped with integrating sphere accessories, with wavelengths ranging from 200 to 800 nm. The absorption spectra were obtained from reflectance using the Kubelka–Munk equation (Equation (1)).[44]

$$F(R_\infty) = \frac{(1-R_\infty)^2}{2R_\infty} = \frac{K}{S} \quad (1)$$

here, $F(R_\infty)$ is the Kubelka–Munk function, R_∞ is the diffuse reflectance, K is the absorption coefficient, and S is the scattering coefficient. Then by

© 2024 The Author(s). Advanced Sustainable Systems published by Wiley-VCH GmbH

RIGHTSLINK

23667486, 2024, 10, Downloaded from https://onlinelibrary.wiley.com/doi/10.1002/adsu.202400375 by Universita Ca' Foscari Venezia, Wiley Online Library on [30/10/2024]. See the Terms and Conditions (https://onlinelibrary.wiley.com/terms-and-conditions) on Wiley Online Library for rules of use; OA articles are governed by the applicable Creative Commons License

exploiting the Tauc method,[45] the bandgap for TiO_2 semiconductors can be expressed using Equation (2):

$$(F(R_\infty)\,h\nu)^{\frac{1}{2}} = B\left(h\nu - E_g\right) \quad (2)$$

here, h is Planck's constant, ν is the frequency of the light, and B is a constant. By plotting $F(R_\infty)$ versus the energy expressed in eV, and by finding the x-axis intersection point of the linear fit of the Tauc plot, it is possible to estimate the bandgap of a material. Photoluminescence (PL) measurements were performed at room temperature and in air, using a FluoroLog 3–21 system (Horiba Jobin-Yvon) equipped with a 450 W xenon arc lamp as excitation source. The wavelength was selected through a double Czerny–Turner monochromator and signal detection stage including an iHR300 single grating monochromator coupled to a Hamamtsu photomultiplier tube (model R928P for visible range; model R5509-73 N2-cooled for NIR range). Excitation wavelength was set to 350 nm and PL spectra were recorded over the range of 380-600 nm.

Rutherford backscattering spectrometry (RBS) was performed using a $^4He^+$ beam with energy E_0 of 2.0 MeV, and the backscattered beam was collected at backscattering angle $\theta = 160°$ in IBM geometry.

Photocatalytic Tests: Photocatalytic activity of the synthesized materials was evaluated following the degradation of ciprofloxacin (CIP), chosen as the target molecule, under simulated solar light. For this purpose, a 100 mL cylindrical concentric Pyrex-quartz photocatalytic reactor under a solar simulator light equipped with a 100 W Xenon arc lamp and AM1.5G filter (Abet Technologies) was used. During the photocatalytic tests, the reactor was located under the solar lamp at a suitable distance to obtain a power of 1 sun (1 kW m^{-2}). The photon flux was measured by using a Si-based reference solar cell #15 150 (Abet Technologies, USA) leaned against the external wall of the photoreactor containing only pure water. The initial concentration (C_0) of the target molecule was 4×10^{-5} M and the amount of photocatalyst was fixed at 125 mg L^{-1}. The photocatalytic tests were performed at room temperature and atmospheric pressure and at pH 5 which was CIP pH aqueous solution. Before irradiation, adsorption-desorption equilibrium was reached by stirring the suspension in the dark for 30 min. The photocatalytic reaction started by switching on the lamp and filtered aliquots of the aqueous suspension were collected at given time intervals, by using a 0.45 mm polytetrafluoroethylene (PTFE) Millipore disc. Drug concentration was measured using a Perkin Elmer Lambda 1050^+ UV–vis–NIR spectrometer, following the CIP absorption maximum peak at 272 nm. Since the degradation pathway for CIP is known and it can be related to pseudo-first-order kinetics,[4] the apparent kinetic constant k was calculated as shown in Equation (3), evaluating the data interval from 0 to 30 min and adopting the pseudo-first-order model:

$$ln\frac{C}{C_0} = -kt \quad (3)$$

where k is the apparent pseudo-first-order rate constant (min^{-1}), calculated as

$$k = 2.303 \times slope \quad (4)$$

The main active species in the CIP degradation were investigated by performing free radical trapping experiments. Briefly, three different photocatalytic tests were carried out using the same conditions as before but adding to the reaction system tert-Butanol (tBuOH, 1 mM), oxalic acid (OA, 1 mM), and nitrogen (N_2 (g)) as hydroxy groups (OH), holes (h^+) and superoxide (O_2^-) scavengers, respectively. Finally, to evaluate the stability and reusability of the photocatalysts, a 3-cycle recycling test was performed. The best performing sample was collected by centrifugation, washed with deionized water several times, and dried overnight after each photocatalytic cycle.

Supporting Information

Supporting Information is available from the Wiley Online Library or from the author.

Acknowledgements

E.R.C., A.I.M., and I.B.M. would like to thank the Spanish Ministry of Science and Innovation, project TED2021-130756B–C31 funded by MCIN/AEI/10.13039/501100011033 and by "ERDF A way of making Europe" by the European Union Next Generation EU/PRTR. A.V. acknowledges the Kempe Foundations, the Knut och Alice Wallenberg Foundation, the Luleå University of Technology (Labfund program), and the European Union – NextGenerationEU – through MUR (National Recovery and Resilience Plan (NRRP) – Mission 4 Component 2, Investment N. ECS00000043 – CUP N. H43C22000540006 (iNEST) and Mission 4 Component 2 Investment 1.3 – CUP D43C22003090001 (NEST)).

Conflict of Interest

The authors declare no conflict of interest.

Data Availability Statement

The data that support the findings of this study are available from the corresponding author upon reasonable request.

Keywords

cerium, drug photodegradation, photocatalysis, TiO_2 nano-octahedra

Received: May 29, 2024
Revised: August 2, 2024
Published online: September 9, 2024

[1] R. P. Schwarzenbach, T. Egli, T. B. Hofstetter, U. v. Gunten, B. Wehrli, *Ann. Rev. Environ. Res.* **2010**, *35*, 109.
[2] M. Farzadkia, E. Bazrafshan, A. Esrafili, J. K. Yang, M. Shirzad-Siboni, *J. Environ. Health Sci.* **2015**, *13*.
[3] M. Patel, R. Kumar, K. Kishor, T. Mlsna, C. U. Pittman Jr., D. Mohan, *Chem. Rev.* **2019**, *119*, 3510.
[4] X. Hu, X. Hu, Q. Peng, L. Zhou, X. Tan, L. Jiang, C. Tang, H. Wang, S. Liu, Y. Wang, Z. Ning, *Chem. Eng. J.* **2020**, *380*, 122366.
[5] A. G. Fane, C. Y. Tang, R. Wang, in *Treatise on Water Science*, (Ed.: P. Wilderer), Elsevier, Oxford **2011**.
[6] V. Kumar, M. P. Shah, in *Advanced Oxidation Processes for Effluent Treatment Plants*, (Ed.: M. P. Shah), Elsevier, Amsterdam, Netherlands **2021**.
[7] M. Pelaez, N. T. Nolan, S. C. Pillai, M. K. Seery, P. Falaras, A. G. Kontos, P. S. M. Dunlop, J. W. J. Hamilton, J. A. Byrne, K. O'Shea, M. H. Entezari, D. D. Dionysiou, *Appl. Catal., B.* **2012**, *125*, 331.
[8] a) P. D. Cozzoli, R. Comparelli, E. Fanizza, M. L. Curri, A. Agostiano, *Mater. Sci. Eng., C.* **2003**, *23*, 707; b) R. Parimaladevi, M. Umadevi, T. N. Rekha, A. M. F. Benial, in *Nanotechnology in the Beverage Industry*, Elsevier, Amsterdam, Netherlands **2020**.
[9] R. Asahi, Y. Taga, W. Mannstadt, A. J. Freeman, *Phys. Rev. B.* **2000**, *61*, 7459.
[10] a) E. B. Simsek, *Appl. Catal., B.* **2017**, *200*, 309; b) A. Khlyustova, N. Sirotkin, T. Kusova, A. Kraev, V. Titov, A. Agafonov, *Mater. Adv.* **2020**, *1*, 1193; c) S. Pany, K. M. Parida, B. Naik, *RSC Adv.* **2013**, *3*, 4976.

© 2024 The Author(s). Advanced Sustainable Systems published by Wiley-VCH GmbH

RIGHTSLINK

23667486, 2024, 10, Downloaded from https://onlinelibrary.wiley.com/doi/10.1002/adsu.202400375 by Universita Ca' Foscari Venezia, Wiley Online Library on [30/10/2024]. See the Terms and Conditions (https://onlinelibrary.wiley.com/terms-and-conditions) on Wiley Online Library for rules of use; OA articles are governed by the applicable Creative Commons License

[11] a) C.-T. Dinh, T.-D. Nguyen, F. Kleitz, T.-O. Do, *ACS Nano* **2009**, *3*, 3737; b) J. Du, J. Zhang, D. J. Kang, *CrystEngComm* **2011**, *13*, 4270; c) E. Hosono, S. Fujihara, H. Imai, I. Honma, I. Masaki, H. Zhou, *ACS Nano* **2007**, *1*, 273; d) L. Liccardo, M. Bordin, P. M. Sheverdyaeva, M. Belli, P. Moras, A. Vomiero, E. Moretti, *Adv. Funct. Mater.* **2023**, *33*, 2212486; e) M. Telkhozhayeva, B. Hirsch, R. Konar, E. Teblum, R. Lavi, M. Weitman, B. Malik, E. Moretti, G. D. Nessim, *Appl. Catal., B.* **2022**, *318*, 121872.
[12] a) T.-Y. Lee, C.-Y. Lee, H.-T. Chiu, *ACS Omega* **2018**, *3*, 10225; b) G. Liu, H. G. Yang, J. Pan, Y. Q. Yang, G. Q. Lu, H.-M. Cheng, *Chem. Rev.* **2014**, *114*, 9559; c) H. G. Yang, C. H. Sun, S. Z. Qiao, J. Zou, G. Liu, S. C. Smith, H. M. Cheng, G. Q. Lu, *Nature* **2008**, *453*, 638.
[13] a) F. Amano, T. Yasumoto, O.-O. Prieto-Mahaney, S. Uchida, T. Shibayama, B. Ohtani, *Chem. Commun.* **2009**, 2311; b) W. Chen, Q. Kuang, Q. Wang, Z. Xie, *RSC Adv.* **2015**, *5*, 20396.
[14] I. Barroso-Martín, E. Moretti, A. Talon, L. Storaro, E. Rodríguez-Castellón, A. Infantes-Molina, *Materials* **2018**, *11*.
[15] Y.-h. Xu, H.-r. Chen, Z.-x. Zeng, B. Lei, *Appl. Surf. Sci.* **2006**, *252*, 8565.
[16] F. B. Li, X. Z. Li, M. F. Hou, K. W. Cheah, W. C. H. Choy, *Appl. Catal., A.* **2005**, *285*, 181.
[17] B. Ohtani, *J. Photochem. Photobiol., C.* **2010**, *11*, 157.
[18] M. D. Donohue, G. L. Aranovich, *Adv. Colloid. Interfac* **1998**, *76–77*, 137.
[19] Z. Y. Yuan, X. B. Zhang, B. L. Su, *Appl. Phys. A.* **2004**, *78*, 1063.
[20] M. Piumetti, S. Bensaid, N. Russo, D. Fino, *Appl. Catal., B.* **2016**, *180*, 271.
[21] M. G. Kim, J. M. Kang, J. E. Lee, K. S. Kim, K. H. Kim, M. Cho, S. G. Lee, *ACS Omega* **2021**, *6*, 10668.
[22] a) G. Greczynski, L. Hultman, *Prog. Mater. Sci.* **2020**, *107*, 100591; b) Y. Li, W. Li, F. Liu, M. Li, X. Qi, M. Xue, Y. Wang, F. Han, *J. Nanopart Res.* **2020**, *22*, 122.
[23] S. Dey, S. C. Roy, *J. Alloy Compd.* **2021**, *881*, 160481.
[24] A. H. Zaki, M.-J. Lee, *ACS Omega* **2019**, *4*, 19623.
[25] S. Watanabe, X. Ma, C. Song, *J. Phys. Chem. C.* **2009**, *113*, 14249.
[26] A. Kotani, T. Jo, J. C. Parlebas, *Adv. Phys.* **1988**, *37*, 37.
[27] M.-K. Lee, Y.-C. Park, *Langmuir* **2019**, *35*, 2066.
[28] M. Pudukudy, Q. Jia, J. Yuan, S. Megala, R. Rajendran, S. Shan, *Mater. Sci. Semicond. Process.* **2020**, *108*, 104891.
[29] N. Zhang, Z. Z. Yang, Z. Chen, Y. X. Li, Y. W. Liao, Y. P. Li, M. C. Gong, Y. Q. Chen, *Catalysts* **2018**, *8*.
[30] E. Bêche, P. Charvin, D. Perarnau, S. Abanades, G. Flamant, *Surf. Interface Anal.* **2008**, *40*, 264.
[31] R. Fiorenza, M. Bellardita, T. Barakat, S. Scirè, L. Palmisano, *J. Photochem. Photobiol. A: Chem.* **2018**, *352*, 25.
[32] N. A. Morozov, D. S. Ershov, O. Y. Sinel'shchikova, N. V. Besprozvannykh, S. V. Mjakin, E. Y. Brazovskaya, O. L. Galankina, A. V. Koroleva, *Appl. Surf. Sci.* **2024**, *644*, 158765.
[33] a) Q. Wang, H. Zhu, B. Li, *Chem. Eng. J.* **2019**, *378*, 122072; b) S. Zhang, H. Liu, F. Gao, M. Fang, Y. Zhang, Y. Cai, K. Li, M. Kong, X. Tan, *J. Alloy Compd.* **2022**, *900*, 163492.
[34] a) A. R. Albuquerque, A. Bruix, I. M. G. dos Santos, J. R. Sambrano, F. Illas, *J. Phys. Chem. C.* **2014**, *118*, 9677; b) M. M. Khan, S. A. Ansari, D. Pradhan, D. H. Han, J. Lee, M. H. Cho, *Ind. Eng. Chem. Res.* **2014**, *53*, 9754.
[35] B. Choudhury, B. Borah, A. Choudhury, *Photochem. Photobiol.* **2012**, *88*, 257.
[36] G. Bahmanrokh, C. Cazorla, S. S. Mofarah, R. Shahmiri, Y. Yao, I. Ismail, W.-F. Chen, P. Koshy, C. C. Sorrell, *Nanoscale* **2020**, *12*, 4916.
[37] S. Xing, T. Li, Y. Gao, J. Liu, *Optik* **2019**, *183*, 266.
[38] C. Alberoni, I. Barroso-Martín, A. Infantes-Molina, E. Rodríguez-Castellón, A. Talon, H. Zhao, S. You, A. Vomiero, E. Moretti, *Mater. Chem. Front.* **2021**, *5*, 4138.
[39] Z. Wei, M. Endo-Kimura, C. Colbeau-Justin, B. Ohtani, E. Kowalska, *J. Nanosci. Nanotechnol.* **2020**, *20*, 1278.
[40] K. Kenchappa Somashekharappa, S. V. Lokesh, *ACS Omega* **2021**, *6*, 7248.
[41] J. Zhang, P. Sun, P. Jiang, Z. Guo, W. Liu, Q. Lu, W. Cao, *J. Mater. Chem. C.* **2019**, *7*, 5764.
[42] M. Sluban, P. Umek, *J. Phys. Chem. C.* **2019**, *123*, 23747.
[43] a) H. Cheng, J. Ma, Z. Zhao, L. Qi, *Chem. Mater.* **1995**, *7*, 663; b) Z. Yanqing, S. Erwei, C. Zhizhan, L. Wenjun, H. Xingfang, *J. Mater. Chem.* **2001**, *11*, 1547.
[44] P. kubelka, F. Munk, *Fuer Tekn. Physik* **1931**, *12*, 593.
[45] P. Makuła, M. Pacia, W. Macyk, *J. Phys. Chem. Lett.* **2018**, *9*, 6814.

© 2024 The Author(s). Advanced Sustainable Systems published by Wiley-VCH GmbH

RIGHTSLINK

23667486, 2024, 10, Downloaded from https://onlinelibrary.wiley.com/doi/10.1002/adsu.202400375 by Universita Ca' Foscari Venezia, Wiley Online Library on [30/10/2024]. See the Terms and Conditions (https://onlinelibrary.wiley.com/terms-and-conditions) on Wiley Online Library for rules of use; OA articles are governed by the applicable Creative Commons License